Seasonal Predictability in a Model Atmosphere

HAI LIN

Department of Atmospheric and Oceanic Sciences and Centre for Climate and Global Change Research, McGill University, Montreal, Quebec, Canada

(Manuscript received 22 June 2000, in final form 27 October 2000)

ABSTRACT

The predictability of atmospheric mean-seasonal conditions in the absence of externally varying forcing is examined. A perfect-model approach is adopted, in which a global T21 three-level quasigeostrophic atmospheric model is integrated over 21 000 days to obtain a reference atmospheric orbit. The model is driven by a time-independent forcing, so that the only source of time variability is the internal dynamics. The forcing is set to perpetual winter conditions in the Northern Hemisphere (NH) and perpetual summer in the Southern Hemisphere.

A significant temporal variability in the NH 90-day mean states is observed. The component of that variability associated with the higher-frequency motions, or climate noise, is estimated using a method developed by Madden. In the polar region, and to a lesser extent in the midlatitudes, the temporal variance of the winter means is significantly greater than the climate noise, suggesting some potential predictability in those regions.

Forecast experiments are performed to see whether the presence of variance in the 90-day mean states that is in excess of the climate noise leads to some skill in the prediction of these states. Ensemble forecast experiments with nine members starting from slightly different initial conditions are performed for 200 different 90-day means along the reference atmospheric orbit. The serial correlation between the ensemble means and the reference orbit shows that there is skill in the 90-day mean predictions. The skill is concentrated in those regions of the NH that have the largest variance in excess of the climate noise. An EOF analysis shows that nearly all the predictive skill in the seasonal means is associated with one mode of variability with a strong axisymmetric component.

1. Introduction

Atmospheric fluctuations on the seasonal and interannual timescales arise as a result of interactions with the underlying surface, as well as from the internal dynamics of the atmosphere itself. It is now well known, for example, that sea surface temperature anomalies (SSTAs) of the El Niño and La Niña type are associated with atmospheric flow anomalies of several months' duration in the Tropics, and to a smaller but still significant extent in some regions of the midlatitudes. In fact, the recent interest in the possibility of predicting mean seasonal conditions is essentially based on this known correlation between tropical Pacific SSTAs and the atmospheric flow (Wallace and Gutzler 1981; Derome et al. 2001). The higher thermal and mechanical inertia of the oceans in comparison with the atmosphere leads to a higher predictability of the oceans, which in turn can hopefully be used to predict the influence of the oceans on the atmosphere.

Independently of the lower boundary forcing, the atmosphere's internal dynamics can also generate some variability in mean-seasonal conditions, as has been shown with models subjected to periodically varying SSTs (e.g., Lau 1981). The main source of this variability resides in the baroclinically active synoptic scales that, through nonlinear processes, spread the variability to all frequencies. A method for estimating the level of the climate noise from a knowledge of the higher frequencies was developed by Madden (1976). The physics can be modeled by a first-order autoregressive process and yields a red frequency spectrum (Hasselmann 1976). The possibility also exists that some internal dynamical mechanism other than the weather noise could generate temporal variability in mean-seasonal states over and above the climate noise. The present study examines this possibility in a simple model.

Madden used a 74-yr dataset of monthly mean sea level pressures over the Northern Hemisphere and compared the observed temporal variance in the monthly mean data with what would be expected to be generated by the weather noise. He found that between 40° and 60°N nearly all the observed variance can be explained by the climate noise, whereas some excess variance could be seen in the subtropics and north of 60°N. It is not possible to see from his results alone, however, what mechanism(s) gave rise to the excess variance, whether

Corresponding author address: Dr. Hai Lin, Department of Atmospheric and Oceanic Sciences and Centre for Climate and Global Change Research, McGill University, 805 rue Sherbrooke ouest, Montreal, PQ H3A 2K6, Canada.
E-mail: hlin@zephyr.meteo.mcgill.ca

the latter was all generated by the external forcing or whether some of it was internally generated.

Zwiers (1987) analyzed the output of a 20.5-yr general circulation model simulation in which the SST was specified to be 1-yr periodic. He found evidence for potential predictability, that is, for excess variance over climate noise, in the winter-mean 500-hPa height and surface pressure. The excess variance over climate noise appeared to be associated with a single event of large amplitude involving an atmospheric mass transfer between the Tropics and the high latitudes of the Southern Hemisphere. There is therefore some evidence that the internal dynamics can generate more low-frequency variability than can be explained by climate noise, although that excess variability is small compared to the climate noise.

The interest in the excess variance over climate noise, whether externally or internally generated, arises from the fact that it is potentially predictable. A number of studies, such as Kumar and Hoerling (1995) and Derome et al. (2001), have shown that the component of the excess variance that is associated with SSTAs of the El Niño and La Niña type contributes to some forecast skill on the seasonal timescale. It is less clear that there is significant excess skill associated with the internal dynamics, and that, if present, it adds to the predictability of the system. In this study we examine these questions in the context of a simple atmospheric model. We examine the low-frequency variability in the global, three-level quasigeostrophic atmospheric model of Marshall and Molteni (1993). Because the model is forced by time-independent sources of potential vorticity, all temporal variability is internally generated. We show that the model has more low-frequency variability than would be expected from the climate noise, an excess variability that projects strongly onto a single mode, or spatial structure, with a distinct axisymmetric component. Using a perfect-model approach, we perform a series of prediction experiments to see whether this potentially predictable variability actually leads to some predictability on the seasonal timescale. We show that this is indeed the case, and that the predictability is highly concentrated in a single mode, the mode with the most excess variance over the climate noise.

A brief description of the three-level quasigeostrophic model and of a long, control run establishing a reference state is given in section 2. In section 3, Madden's (1976) technique is used to estimate the weather noise variability and the excess, potentially predictable, variability in 90-day means of the 500-hPa geopotential height. Section 4 describes the setup of the seasonal prediction experiments. A number of 90-day predictions are conducted by adding small perturbations to the first day of each 90-day period in the control run, and the predictive skill of the seasonal means is analyzed in section 5. In section 6, relation between the seasonal predictive skill and flow patterns is explored, where the flow patterns are defined as a number of empirical othogonal function (EOF) modes. It is found that the first EOF mode that is characterized by a zonally symmetric structure has the highest predictive skill. In section 7, the behavior of the first EOF mode and its dynamics are discussed. Section 8 gives a summary and conclusions.

2. The model and control run

This study is based on the spectral, three-level quasigeostrophic model of Marshall and Molteni (1993). The model has a global domain with pressure as the vertical coordinate and a triangular 21 (T21) horizontal resolution. The prognostic equations for the quasigeostrophic potential vorticity are written at 200, 500, and 800 hPa. The dissipative terms include the effects of Newtonian relaxation of temperature, linear drag on the 800-hPa wind, and horizontal diffusion of vorticity and temperature. The forcing terms are time-independent but spatially varying sources of potential vorticity calculated from winter observations. Our model differs from the original version provided by Marshall and Molteni only in that the forcing functions were recalculated with nine winters (1980/81–1988/89) of the European Centre for Medium-Range Weather Forecasts analyses. The earth's orography is explicitly represented so that the flow can interact with it. In spite of its limitations, such as having no moisture variable, in the Northern Hemisphere this model has remarkably realistic stationary planetary waves and the broad climatological characteristics of the transients are in general agreement with observations (Lin and Derome 1996, 1999). The Southern (summer) Hemisphere climatology is less realistic, but all results to be presented in this paper are from the Northern Hemisphere.

We begin by performing an integration of 21 450 days in perpetual NH winter mode. The initial spinup period of 450 days is discarded and for the remaining period the streamfunction is saved daily. The 21 000 days of model data are divided into 200 independent 90-day periods, ''winters,'' by omitting the first 15 days and the 15 days between consecutive 90-day periods. As will be seen in section 4, the information in the omitted periods will be used in the tangent linear model to get initial errors for the forecasting experiments. For ease of presentation, we will refer to the variability among the 90-day means or winters as being ''interannual.'' The streamfunction is converted into geopotential height with the linear balance equation. The output Gaussian grid data are converted to latitude–longitude grid data with a resolution of $5^\circ \times 5^\circ$. In the following discussions we will focus on the 500-hPa geopotential height field north of 20°N.

3. Potential predictability

The variance among the nonoverlapping 90-day means, denoted $V_{\bar{z}}$ can be expressed as

$$V_{\bar{z}} = V_{\bar{z}_n} + V_{\bar{z}_s}, \tag{1}$$

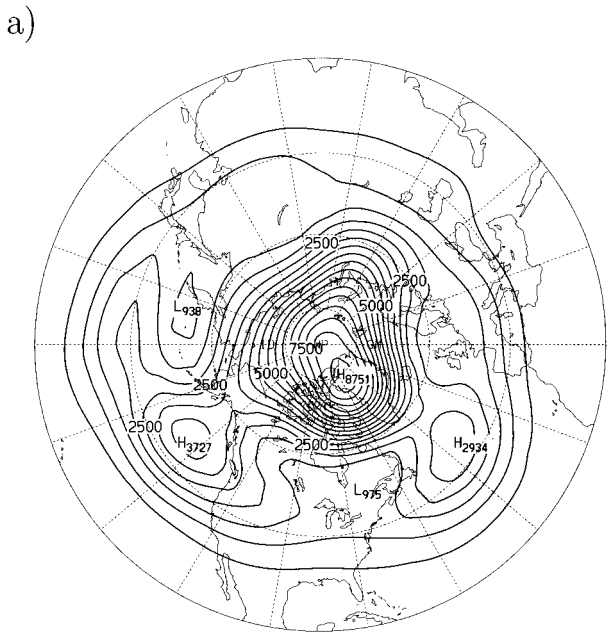

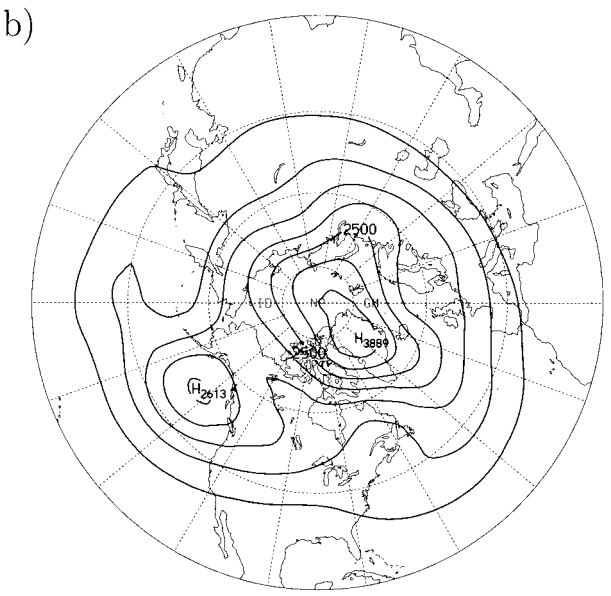

FIG. 1. (a) Actual variance of 90-day-averaged 500-hPa geopotential height from a 200-winter control run; (b) variance of natural variability estimated from a statistical method; (c) difference between (a) and (b). The contour intervals are 500 m^2.

where $V_{\overline{z}_n}$ is the climate noise variance and $V_{\overline{z}_s}$ is the excess variance, internally generated by dynamical processes. Here $V_{\overline{z}}$ can be computed directly from the time series of N 90-day means, that is,

$$V_{\overline{z}} = \frac{1}{N}\sum_{j=1}^{N} (\overline{z}_j - [\overline{z}])^2, \qquad (2)$$

where $\overline{z}_j$, $j = 1, 2, \ldots, N$ is the 90-day mean for year j, and $[\overline{z}]$ is its average over N years. In our case, $N = 200$.

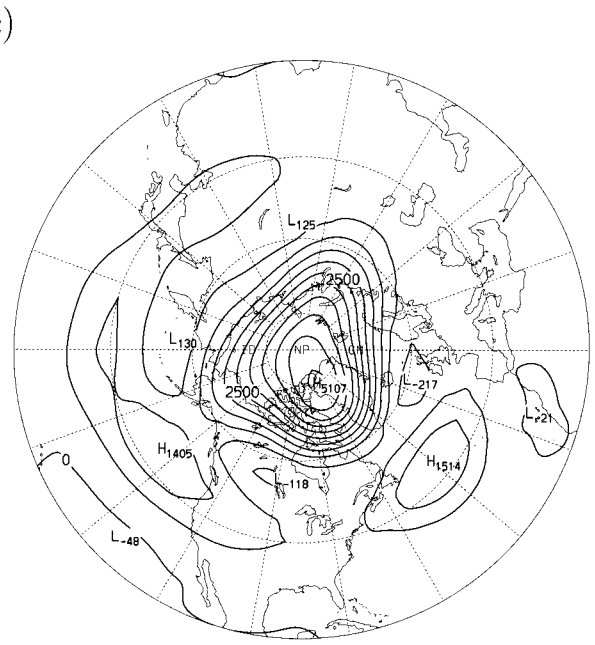

FIG. 1. (*Continued*)

Here $V_{\overline{z}_n}$ is estimated in a way similar to Zwiers (1987) as described in the appendix. In this method, a 90-day period of daily data is Fourier analyzed to obtain its power spectrum. The spectrum is extended to zero frequency by a low-frequency white noise approximation (LFWN), the response of a 90-day mean filter is applied to the spectrum, and the power of the 90-day mean is obtained by a discrete integral over frequency. This is done for each of the 200 periods of 90 days and the results are averaged. The $V_{\overline{z}}$, $V_{\overline{z}_n}$, and their difference $V_{\overline{z}_s}$ are calculated at all available grid points and maps of the results are plotted.

Figure 1a shows $V_{\overline{z}}$ for 90-day means in the 500-hPa geopotential height. The variance is seen to increase with latitude, reaching a maximum near the Pole and over northern Greenland. In the middle latitudes, local maxima are observed over the northeast Pacific and the North Atlantic. Figure 1b depicts the climate noise variability $V_{\overline{z}_n}$. A similar distribution as in Fig. 1a is seen, but with generally smaller values. Figure 1c shows the potentially predictable variance $V_{\overline{z}_s}$, obtained as the difference between Figs. 1a and 1b.

To estimate the statistical significance of the variance shown in Fig. 1c we compute the F ratio $F = V_{\overline{z}}/V_{\overline{z}_n}$, from Figs. 1a and 1b and test if F is significantly different from one. Because we have $N = 200$ 90-day means, the significance level of F being different from unity is computed using $N - 1 = 199$ degrees of freedom (dof) for $V_{\overline{z}}$. In obtaining $V_{\overline{z}_n}$ we have averaged 200 estimates of $V_{\overline{z}_n}$, each having 2 dof, resulting in $2N = 400$ dof for the average $V_{\overline{z}_n}$ (Zwiers 1987).

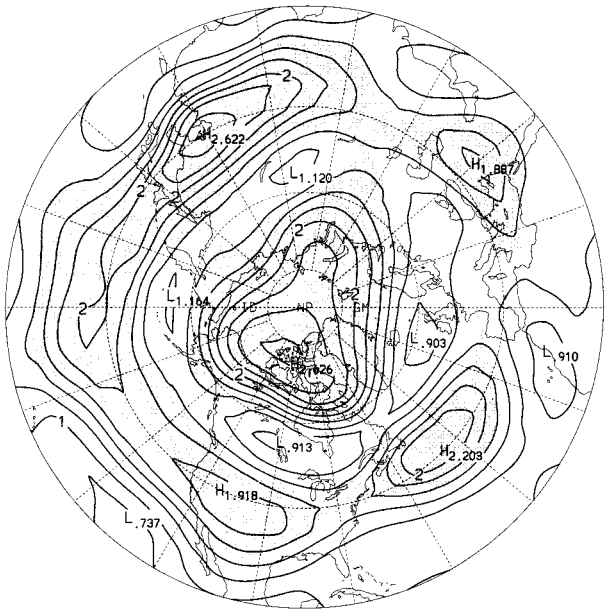

FIG. 2. Ratio of actual variance to variance of natural variability. Regions where the ratio is significantly greater than 1 at 1% significance level from an F test are shaded.

Figure 2 shows the map of F, with shading indicating statistical significance at the 1% level or better. We see a strong evidence of potential predictability in the polar region and along about 40°N latitude. Madden (1976) had also obtained a region of potential predictability near the Pole when working with monthly means of mean sea level observations. Similarly, Zwiers (1987) also found a polar region of predictability in seasonal means of 500-hPa height data from a GCM. Neither, however, found significant potential predictability in the midlatitudes. The difference in our midlatitude results with theirs may have several sources. We use a dry quasigeostrophic model rather than observations or a GCM and we use a longer data record. As will be seen later, the variability in the polar area is part of a dominant zonally symmetric flow pattern that has a beltlike center along the midlatitudes.

In the following we conduct a set of prediction experiments that last 90 days. An analysis of the forecast skill and its distribution will be compared with the potential predictability.

4. The forecast experiments

A ''perfect-model'' approach is used in this study. The perpetual-winter control run discussed above will serve as a proxy for the atmospheric observations. This would constitute a realization of 200 winters. Another nine realizations of 200 winters are constructed as predictions of the control run. Each prediction is made in such a way that starting from the first day of every winter, a 90-day integration is performed by adding a small perturbation error to the initial condition.

To obtain the initial error, a similar breeding method as used in Houtekamer and Derome (1994) and Lin and Derome (1996) is used. The breeding method was first introduced by Toth and Kalnay (1993). Instead of using a nonlinear approach as in Toth and Kalnay, we use the tangent linear model method. As discussed by Houtekamer and Derome (1994), these two methods would yield similar bred modes. Starting from 11 days before the first day of each winter, a tangent linear model is initialized with random numbers assigned to the amplitudes of the spherical harmonic coefficients and integrated for 11 days to obtain the ''bred'' perturbation. The tangent linear model is the same model used to generate the reference orbit, but now linearized about the reference, time-dependent atmospheric state. The nature of the bred modes was discussed in Houtekamer and Derome (1994). Because of the fact that the initial random perturbations will amplify most in directions that provide maximum growth, by the end of 11-day period the bred perturbations would be aligned in the directions of the fastest sustainable growth in the model.

The bred perturbation streamfunction is scaled to have a globally and vertically integrated rms value equal to 1% of the model climatological rms value of the total transient part of the streamfunction. The latter was obtained from a previous 5-yr integration of the model and found to be 2.5×10^{-3} in the units of $2\Omega a^2 = 0.59 \times 10^{10}$ m^2 s^{-1}, where Ω is the angular velocity of the earth and a the earth's radius. At the first day of each winter, the perturbation is added to the reference sate to yield the initial condition of that winter for the forecast experiment.

5. Forecast skill

Discussions of the skill of day-to-day weather predictions of the same model can be found in Houtekamer and Derome (1994, 1995) and Lin and Derome (1996). In general, because of error growth the instantaneous weather information is not predictable beyond about 15 days. Here we will focus on predictions of time mean flows during longer periods where instantaneous information is not required.

Because the external forcing is fixed in our QG model, all the possible forecast skill comes from the initial conditions. As introduced in the last section, we have a total of 10 realizations of the 200 winters that include a control run and nine perturbation experiments. Under the perfect-model setup of our experiments, we can assign one of the 10 runs as the ''observed'' realization of the QG model's 200 winter climate and use the remaining nine integrations to construct an ensemble forecast of the assigned run. Cross correlation over the 200 winters between the ''observations'' and the ensemble forecasts is calculated as an indicator of the forecast skill. This is repeated 10 times, taking each realization in turn as the observed run. The results reported in the following are averages of the 10 correlations.

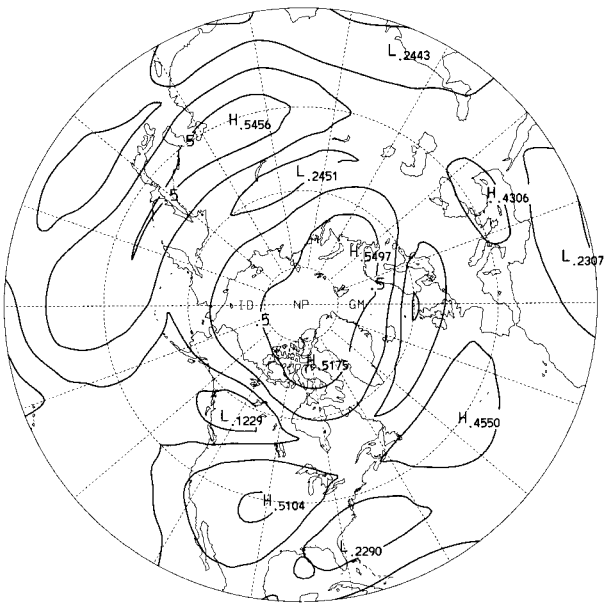

FIG. 3. Correlation coefficients between observed seasonal mean 500-hPa geopotential height and that of ensemble forecasts. The contour interval is 0.1.

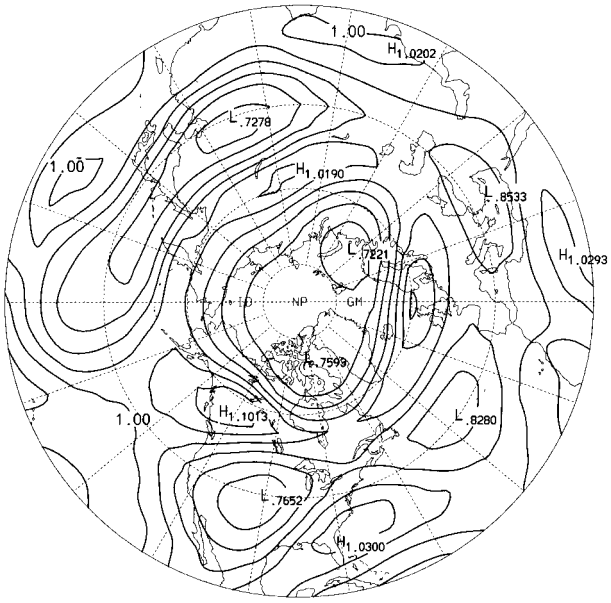

FIG. 4. Relative error variance of the seasonal mean 500-hPa geopotential height forecast.

We first look at the forecast skill of the 90-day seasonal mean 500-hPa geopotential height, as shown in Fig. 3. Highly significant correlations between the observations and the ensemble forecasts are found over the polar area and places along the midlatitudes. A comparison with Fig. 2 shows that the distribution of the forecast skill agrees very well with that of the potential predictability. This indicates that skill in the predictions of the seasonal means does come from some general quantity characterizing the initial conditions.

Another way to measure the forecast skill is the relative error variance, which is defined as the ratio between the error variance of the ensemble forecasts and the variance of the seasonal means. Again each of the 10 realizations is taken as the observations in turn, and the remaining nine runs are used to make an ensemble forecast. Figure 4 shows the relative error variance of forecast of the 90-day seasonal mean 500-hPa geopotential height averaged for the 10 combinations. Small relative error variance of the seasonal mean forecasts occur over the polar area and the midlatitudes along about 40°N. Its distribution is virtually the same as that of the correlation coefficients in Fig. 3.

Forecast skill can also be measured by the spread among the ensemble members. When the ratio of spread to climate variance is calculated (not shown), the distribution is found to be similar to Fig. 4.

It can be demonstrated that in a perfect model approach where the forecast and the observation have the same climate and variance, the cross correlation and the relative error variance have the same meaning in measuring the average forecast skill. They are related by

$$\mathrm{RE} = 2 - 2r, \tag{3}$$

where r is the cross-correlation coefficient between forecast and observation, and RE is the relative error variance.

It can also be shown that in a perfect-model approach when each of the realizations is taken as the observation in turn and compared with the mean of the rest, the average spread among ensembles is linearly related to the averaged error variance.

Based on the above discussions, in the following we will choose to only use the cross correlation to represent the forecast skill.

As reported in Houtekamer and Derome (1995) and Lin and Derome (1996) using the same model, the limit of predictability for day-to-day weather events in this model is about 12 days. Predictive skill coming from the deterministic period must have contributed to the forecast skill of the 90-day seasonal means reported above. To see if there is skill beyond that period, in Fig. 5 we show the forecast skill of the 500-hPa geopotential height averaged over the last 70 days of each winter. Areas with a statistical significance level over 99% estimated by a Student's t test are shaded. Again, significant correlations are found over the polar area and along about 40°N latitude. The maximum correlation coefficients appear to be around 0.34. Therefore, up to 12% of the variance in the observed time means can be predicted using the ensemble forecast. This result implies that the long-range potential predictability obtained from the statistical method is section 3 can be reproduced to some extent from numerical model integrations. It also confirms that Madden's approach does pro-

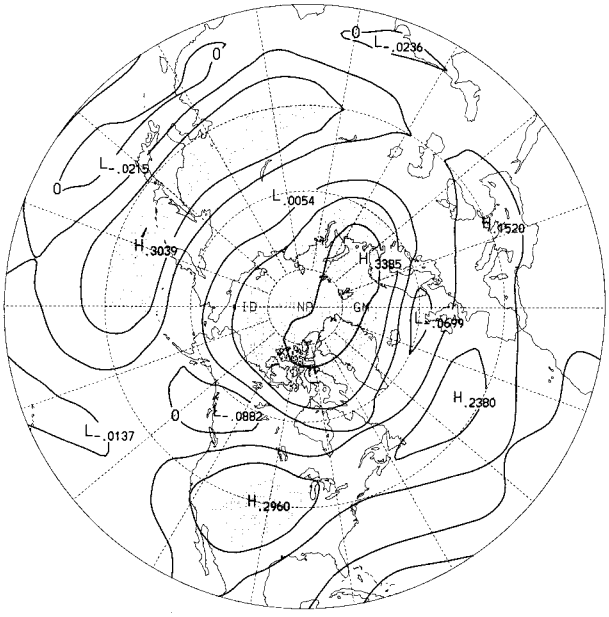

FIG. 5. As in Fig. 3, but for the last 70 days of each winter.

vide useful information on where we can expect long-range predictability to occur.

6. Relation between predictability and flow patterns

In the last section, we saw that there is significant skill in predicting the seasonal means even in an atmosphere with fixed external forcing. The distribution of the predictability shows a somewhat zonally symmetric structure with more skill in the polar area and along the midlatitudes. In this section we investigate if this predictability is associated with some specific flow patterns. As might be expected, a flow with large-scale and long-lived structure would be easier to predict than those smaller scale and more transient ones. We will see if some flow components are systematically forecast more accurately than others.

In order to get a base of independent flow patterns, an EOF decomposition is applied to the 200 winter seasonal mean 500-hPa height fields of the control run. The geographical domain for the EOF analysis extends from 20° to 80°N for all longitudes. The 252 grid points are used with a resolution of 10° lat × 10° long. The effect of unequal areas represented by different grid points is taken into account by multiplying the seasonal mean height fields by the square root of the cosine of latitude at that grid point.

Figure 6 depicts the spatial structure of the first four EOFs. The first mode (E1) accounts for a remarkable 48.6% of the variance and is characterized by a nearly zonally symmetric structure, with out-of-phase oscillations between the heights in the polar region and the midlatitudes. The first mode of an EOF analysis of January monthly mean sea level pressure fields by Wallace and Gutzler (1981) also had a strong zonally symmetric component. We note that our E1 mode has a negative center over Greenland and bands of positive values across the Atlantic and Pacific. Over the Atlantic the mode has some similarity with the North Atlantic oscillation, while the overall structure is reminiscent of the Arctic oscillation discussed by Thompson and Wallace (1998). The second mode (E2) has a structure with some similarity to the Pacific–North America pattern, although more hemispheric in extent. The third mode (E3) has a north–south seesaw in the western Pacific, as the western Pacific mode of Wallace and Gutzler. The E4 mode is more wavelike in the midlatitudes, and explains only 6.4% of the variance.

Now the forecast skill is calculated for each EOF mode. As in the last section, verifications are done for each combination of observations and ensemble forecasts. We project the 200 observed seasonal means onto a given EOF and get a time series of projection coefficients. Similarly we project the 200 ensemble forecasts onto the same EOF and get another time series of projection coefficients. Serial correlation between these two time series would yield a score of the forecast skill for the given EOF. Again the results shown below are averages for the 10 combinations of observations and ensemble forecasts.

Figure 7a displays the forecast skill for 90-day seasonal means for EOFs with indices from 1 to 10. A general trend of decrease of skill with the increase of EOF index can be observed. Here E1 has an outstanding score of over 0.5 as compared with that of other EOFs that are around 0.25. The correlation of projection is statistically significant at 99% level if it is greater than 0.18. The large drop of skill from E1 to other EOFs makes E1 the major contributor to predictability of the seasonal mean flows. Indeed, forecast skill distributions in Figs. 3 and 4 reflect the contribution from the first EOF mode.

The forecast skill of the 500-hPa geopotential height averaged over the first 20 days and that over the last 70 days of each winter as a function of EOF index are shown in Figs. 7b and 7c, respectively. During the first 20 days, forecasts for all EOF modes shown are good (Fig. 7b), and the decrease of skill with EOF index is very clear. For the last 70 days (Fig. 7c), E1 appears to be the only mode to have significant forecast skill.

The zonally symmetric structure of E1 with out-of-phase oscillations between the height anomaly in the polar region and that in the midlatitudes implies an oscillation in the zonal wind along about 60°N. In the context of a quasigeostrophic channel model, Tung and Rosenthal (1986) presented results showing that the zonal index is probably predictable beyond the predictability limit of about 10 days. Using a two-layer primitive equation model with zonally homogeneous boundary conditions, Robinson and Qin (1992) studied the predictability of the zonal index. They found that the

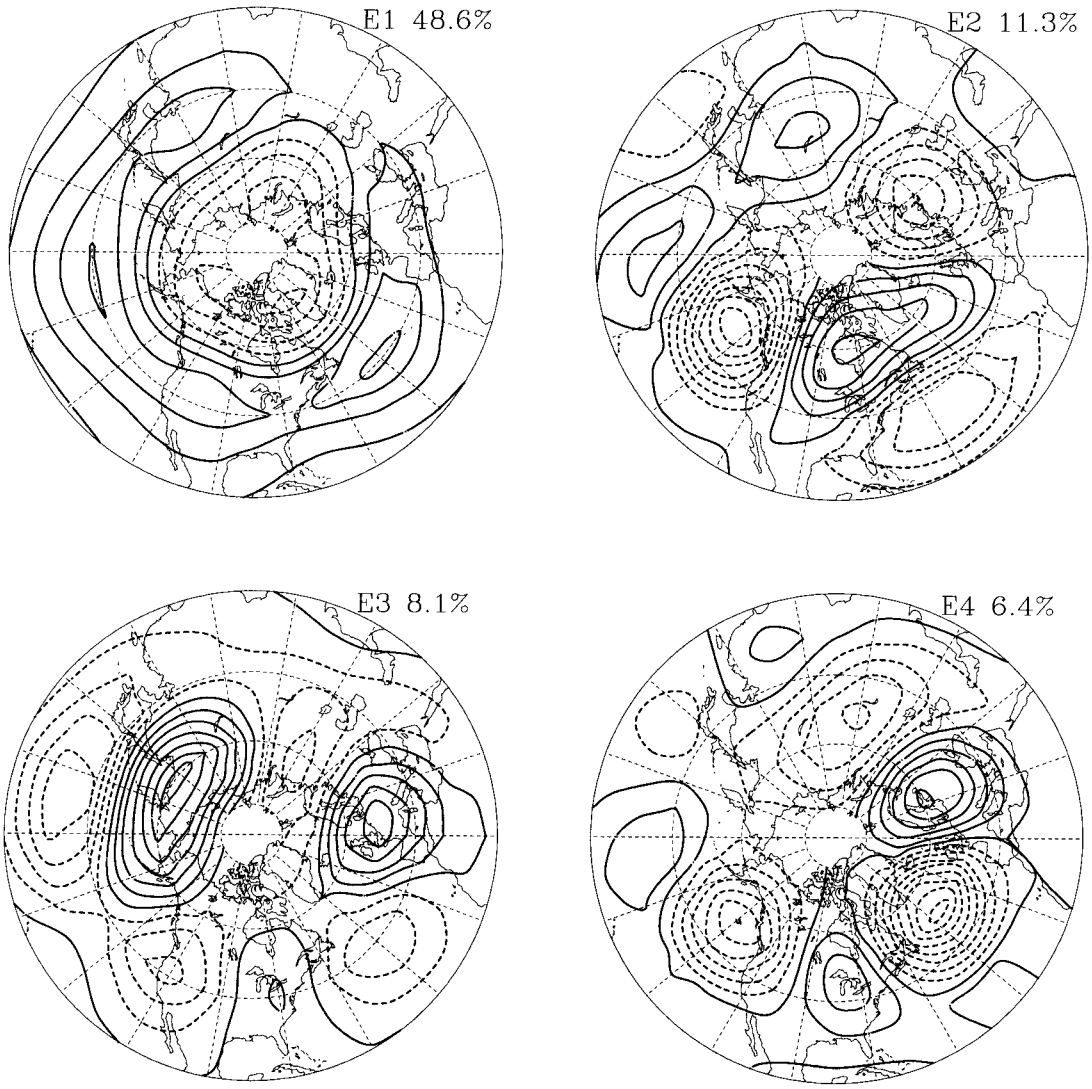

FIG. 6. Distributions of four leading EOFs of the interannual variability of the seasonal mean 500-hPa geopotential height.

zonal index is predictable with useful skill out to about 23 days, significantly more predictable than the overall barotropic flow.

7. Behaviors of E1

Comparing the structure of the E1 mode in Fig. 3a with that of the potentially predictable variance in Fig. 1c, it is evident that the two are closely related. Nearly every local maximum and minimum in the E1 structure matches a maximum in the map of potentially predictable variance.

In order to get some idea on what causes the long-range predictability in the QG model, the behavior of E1 is analyzed in this section. The control run is extended to 31 500 days, and it is divided into 350 continuous 90-day periods. This will allow us to see the time evolution of E1.

The time series, or principal component, of the E1 mode, denoted PC1, presented in Fig. 8 shows pronounced negative spikes but no positive ones of similar magnitudes. This implies intermittent extreme excursions of the negative phase of E1. The time series is therefore not random, as would be the case if it was generated by the weather noise, but is clearly skewed. The frequency spectrum (not shown) from the multitaper spectral analysis (Mann and Lees 1996) has sharp peaks at frequencies corresponding to periods of around 1500 days and 250 days, well above the 5% confidence level. This may indicate that the high recurrence rate of the intermittent excursions has some preferred broadband periods. In the following we examine the dynamics that allows PC1 episodically to reach large negative values.

To get some understanding of the mechanism(s) leading to sharp negative peaks in PC1 (Fig. 8) we began

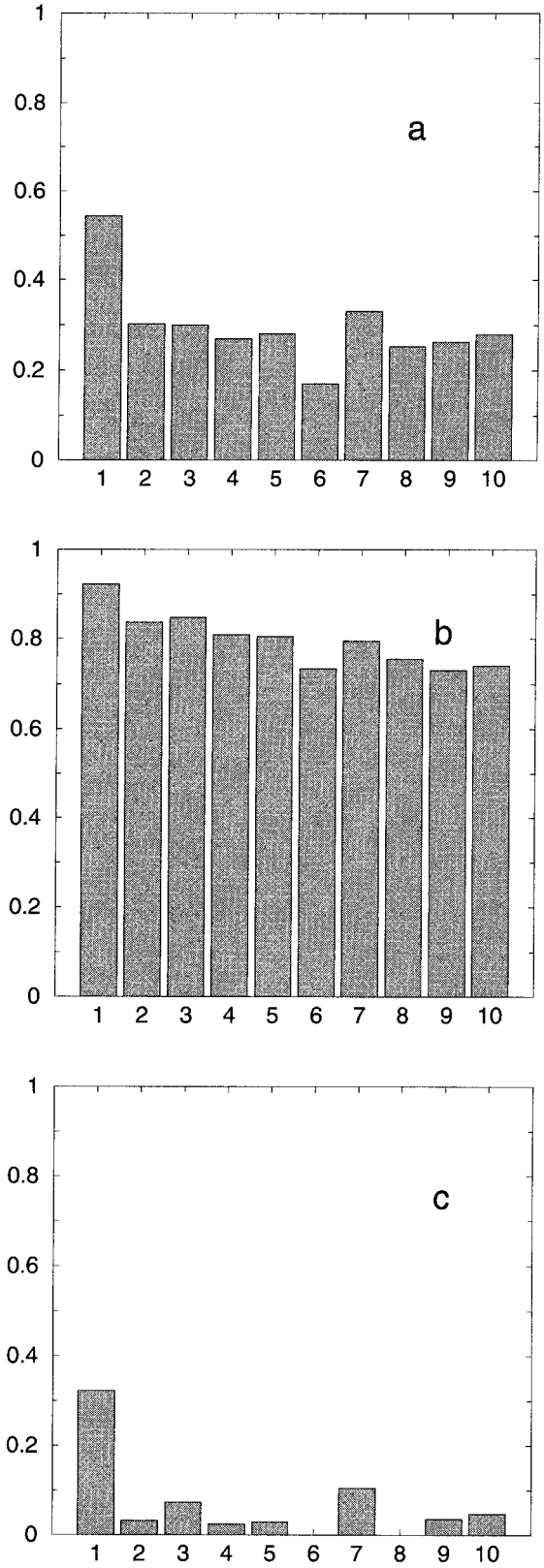

FIG. 7. Forecast skill as a function of EOF index. (a) Forecast of 90-day averages; (b) forecast of the first 20 days; (c) forecast of the last 70 days.

by identifying all periods during which PC1 was undergoing a rapid and large decrease. We selected all sequences of three consecutive PC1 values (always referring to 90-day means) that decreased from the first to the second and from the second to the third period. We also required that the decrease from the first to the third period be larger in magnitude than 0.5 standard deviation of the PC1 time series. Subsequent calculations were done with the 50 resulting central periods, referred to as the growth periods.

To illustrate the mechanisms in action during the decay phase of the strongly negative PC1 mode, we proceeded to identify those periods during which the PC values were increasing rapidly. This was done by applying the same algorithm as for the growth periods, but now requiring the PC1 to be increasing rather than decreasing.

The composites of the 90-day mean 500-hPa height fields during the growth and decay phases are shown in Fig. 9 as deviations from climatology. A comparison with Figs. 9a and 9b reveals that during the growth phase the EOF2 mode dominates the flow, whereas during the decay phase the signature of the decaying EOF1 mode dominates. It appears then that the EOF2 mode plays a role in the growth of the EOF1 mode. The fact that Figs. 9a and 9b are not like each other strongly suggests that the growth of the EOF1 structure is not linear in time, because if it were, one would expect the importance of the EOF1 mode to be similar during the growing and decaying phases. From the counterparts of Fig. 9a at 200 and 800 hPa, (figures not shown), it is seen that the vertical structure of the ''building'' pattern is equivalent barotropic.

We also examined the different dynamical contributions to the growth and decay of EOF1. The same quasigeostrophic potential vorticity equations as used in the QG model is used, for example,

$$\frac{\partial q}{\partial t} = -J(\psi, q) - D + F, \tag{4}$$

where q is potential vorticity, ψ is streamfunction, J is Jacobian operator, F is time-independent forcing, and D is dissipation. Here q at the lowest level includes the topographic effect. For a 90-day average, the above equation becomes

$$\frac{\partial \overline{q}}{\partial t} = -J(\overline{\psi}, \overline{q}) - J(\psi_h, q_h) - J(\psi_l, q_l) - \overline{D} + F, \tag{5}$$

where the overbar is a 90-day average. The subscripts h and l stand for transients of high and low frequencies, meaning periods from 2 to 10 days, and 10 to 90 days.

Terms in (5) are calculated for every 90-day period. The 90-day mean of the potential vorticity tendency can thus be associated with the advection by the time-mean flow of the time-mean variables (vorticity and sensible heat) and of topography, the time-mean of the advection of transient variables by the transient wind (periods of

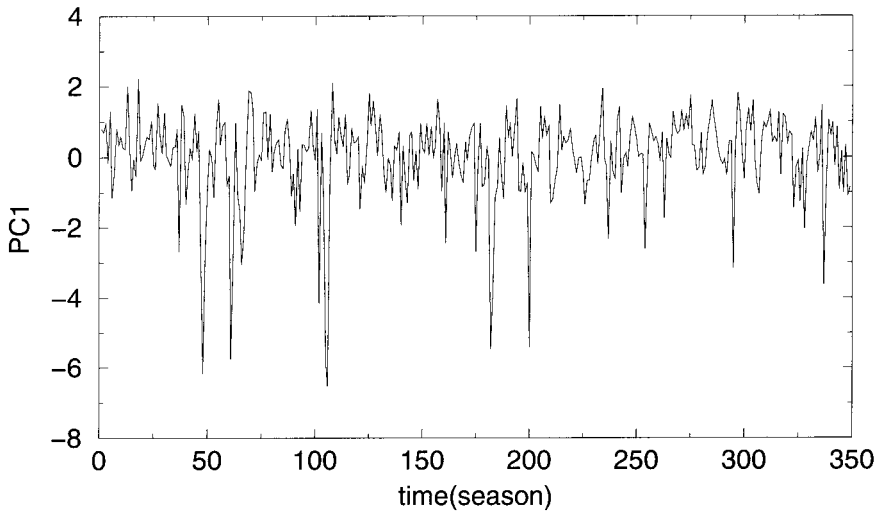

FIG. 8. Time evolution of the amplitude of E1.

90 days and less), as well as the time-independent forcing.

Composites of each term of (5) in the above-defined growth and decay periods of PC1 spikes are calculated. An inverse Laplacian is applied to convert them to height tendencies. In the following we show the departure of the composites from climate.

As the EOF1 is dominated by a zonally symmetric component, we present only the zonally averaged component of (5). Here departures from climate are used, so the last term makes no contribution because it is time independent. Figure 10a shows each of the terms in (5) as a function of latitude, at 500 hPa, for the growth phase of (negative spikes) of EOF1. The main term contributing to the net height tendency (heavy solid line) is the advection of the time-mean variables by the time-mean flow, that is, by the stationary waves. The height tendency due to the high-frequency eddies is smaller, but significant. The tendencies associated with the topography, the low-frequency eddies and the dissipation are relatively small.

The dynamics during the decay phase, depicted in Fig. 10b, is radically different. Here the dissipation is the dominant contribution. We note that as the dissipation is linear in the streamfunction, the zonally averaged dissipation is important in this context only when the zonally averaged streamfunction is significant, which is the case during the decay phase (Fig. 10b) but not during the growth phase (Fig. 9a), which is why the dissipation term is small in the growth phase (Fig. 10a).

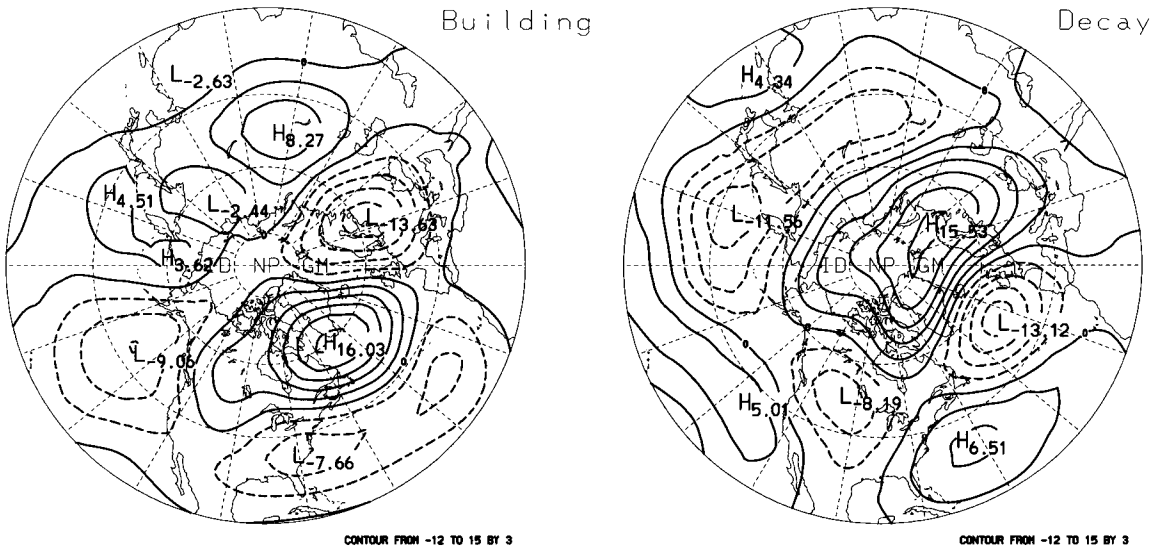

FIG. 9. (a) Composite of 500-hPa height anomalies for growing phase of negative E1 spikes. (b) Composite of 500-hPa height anomalies for decaying phase of negative E1 spikes. Contour intervals are 3 m.

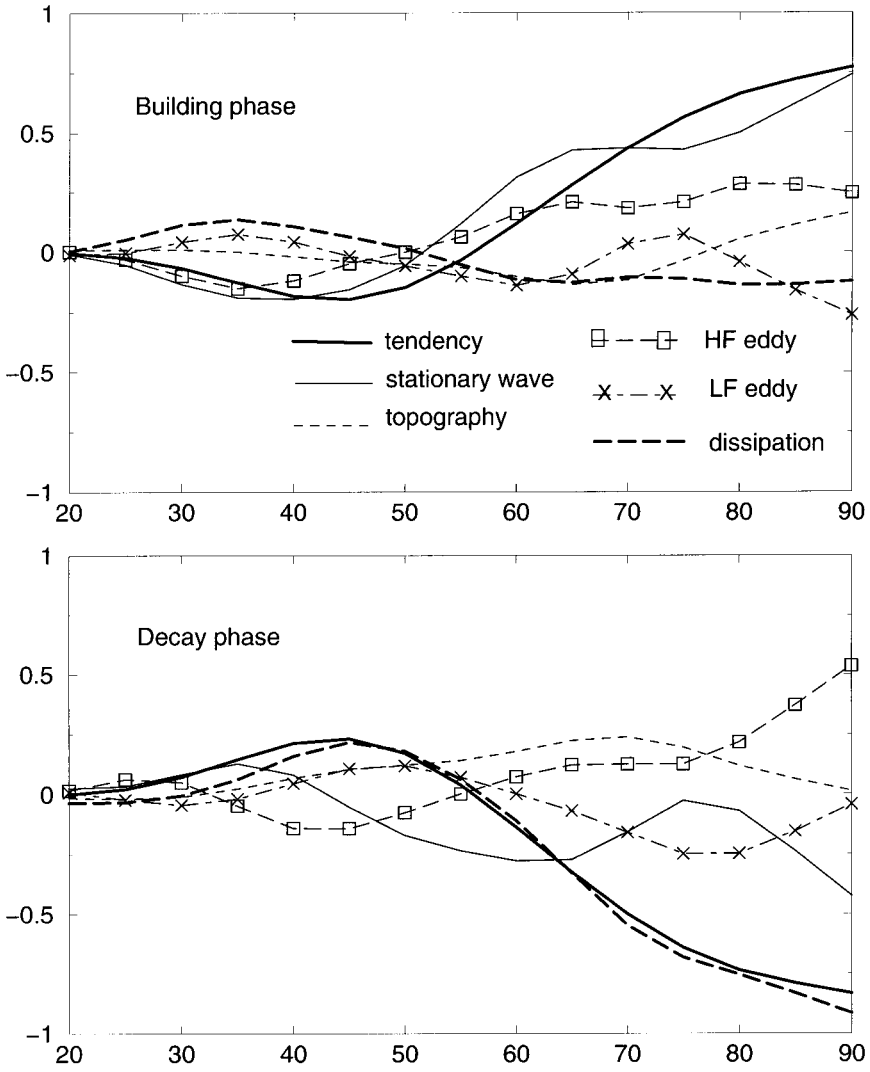

FIG. 10. Composite of 500-hPa height tendencies by different contributions for (a) growing phase and (b) decaying phase (m day^{-1}).

The contribution by the time-mean flow during the decay phase is one of reducing the positive heights near the Pole, as opposed to its positive contribution during the growth phase.

8. Summary and conclusions

A three-level QG model with time-independent external forcing is used to study the potential and actual predictability of the seasonal means. The long perpetual winter integration contains large amounts of ''interannual'' variability despite the absence of any external forcing. Not all of this variability comes from the climate noise that derives from short timescale fluctuations. The excess part is potentially predictable. Strong evidence of potential predictability is found in the polar region and along about 40°N latitude.

An ensemble of seasonal predictions is conducted with different small perturbations in the initial conditions. As the external forcing is time independent, all the possible forecast skill comes from the initial conditions. Serial correlations between the ''observed'' seasonal means and the ensemble forecasts show that there is forecast skill in the polar region and along the midlatitudes. The distribution of the skill is similar to the potential predictability as obtained from the statistical study.

An EOF decomposition is performed on the seasonal mean 500-hPa height fields. The first mode (E1) has mainly a zonally symmetric structure with out-of-phase oscillations between the height anomaly in the polar region and that in the midlatitudes. Correlation of projection for each of the EOF modes is calculated between the observed seasonal means and the ensemble forecasts. There is a general trend of decrease of skill with the increase of EOF index. The E1 has the highest pre-

dictive skill, contributing most of the skill for the whole seasonal forecast and is the only mode that has significant forecast skill for forecast beyond the deterministic period of 20 days.

The time evolution of the amplitude of E1 shows that some strong anomalies can persist over several months. There exist occasional spikes to the large negative values in the time series. This persistence and asymmetry features of the E1 time coefficients are believed to contribute to the potential predictability of the seasonal means of E1 as well as the total fields, since they are not likely to be related to the climate noise.

Some aspects revealed in this study may be worth further investigations. The E1 has a similar structure as the Arctic oscillation (AO) observed in the atmosphere, albeit with higher amplitude. If these two modes share the same dynamical origin, there may be some long-range potential predictability with the AO. Whether such predictability exists in the atmosphere and in general circulation models is of great interest.

Acknowledgments. This research was supported by research grants from the Natural Sciences and Engineering Research Council and the Atmospheric Environment Service of Canada. The author would like to thank Prof. Jacques Derome for helpful discussions.

APPENDIX

Estimation of Climate Noise

Estimation of the climate noise is made following the technique of Madden (1976) and Zwiers (1987). Suppose we have a time series of daily observation z_i, $i = 1, 2, \ldots, 90$. It has a power spectrum density function $S_z(f)$, which can be estimated from a Fourier transform and is normalized so that

$$\int_0^{0.5} S_z(f)\, df = V_{\text{total}}, \tag{A1}$$

where V_{total} is the total variance of daily data within the 90-day period.

We construct another time series y_i by doing an M-day running average to z_i. The spectral density function of y_i can be expressed as

$$S_y(f) = S_z(f)H^2(f), \tag{A2}$$

where transfer function of system

$$H^2(f) = \frac{\sin^2 \pi f M}{\sin^2 \pi f}. \tag{A3}$$

Therefore, the variance of the M-day average is

$$V_{\bar{z}_n} = \int_{-\infty}^{\infty} S_y(f)\, df = \int_{-\infty}^{\infty} S_z(f)H^2(f)\, df. \tag{A4}$$

An LFWN is used to estimate the spectral density of zero frequency $S_z(0)$. Therefore,

$$S_z(0) = S_z(1/90). \tag{A5}$$

The variance of the M-day averages is estimated by evaluating the discrete form of (A4), that is,

$$V_{\bar{z}_n} = \frac{S_z(0)H^2(0)}{180} + \frac{1}{90} \sum_{f=1/90}^{0.5} S_z(f)H^2(f). \tag{A6}$$

When we chose $M = 90$, we have $H^2(0) = 1$ and $H^2(f) = 0$ for $1/90 \geq f \leq 0.5$. Then, the variance of the M-day averages is reduced to

$$V_{\bar{z}_n} = \frac{S_z(0)}{180}. \tag{A7}$$

For each grid point, the above procedure is carried out for each 90-day seasonal time series, resulting in $N(=200)$ independent estimates of climate noise. Each estimate of $V_{\bar{z}_n}$ has 2 dof. For the average of $V_{\bar{z}_n}$ over N seasonal periods, we have a total of $2N(=400)$ dof. The estimate of the actual interannual variability by (2) has $N - 1(=199)$ dof. Their ratio

$$F = \frac{V_{\bar{z}}}{V_{\bar{z}_n}} \tag{A8}$$

will be approximately distributed as an F-random variable with $N - 1$ and $2N$ dof under the null hypothesis that there is no potential predictable signal.

REFERENCES

Derome, J., and Coauthors, 2001: Seasonal predictions based on two dynamical models. *Atmos.–Ocean,* in press.

Hasselmann, K., 1976: Stochastic climate models. Pt. 1: Theory. *Tellus,* **28,** 473–485.

Houtekamer, P. L., and J. Derome, 1994: Prediction experiments with two member ensembles. *Mon. Wea. Rev.,* **122,** 2179–2191.

——, and ——, 1995: Methods for ensemble prediction. *Mon. Wea. Rev.,* **123,** 2181–2196.

Kumar, A., and M. P. Hoerling, 1995: Prospects and limitations of atmospheric GCM climate predictions. *Bull. Amer. Meteor. Soc.,* **76,** 335–345.

Lau, N.-C., 1981: A diagnostic study of recurrent meteorological anomalies appearing in a 15-year simulation with a GFDL general circulation model. *Mon. Wea. Rev.,* **109,** 2287–2311.

Lin, H., and J. Derome, 1996: Changes in predictability associated with the PNA pattern. *Tellus,* **48A,** 553–571.

——, and ——,1999: The genesis and predictability of persistent Pacific–North American anomalies in a model atmosphere. *Tellus,* **51A,** 686–697.

Madden, R. A., 1976: Estimates of the natural variability of time averaged sea level pressure. *Mon. Wea. Rev.,* **104,** 942–952.

Mann, M. E., and J. M. Lees, 1996: Robust estimation of background noise and signal detection in climate time series. *Climatic Change,* **33,** 409–445.

Marshall, J., and F. Molteni, 1993: Toward a dynamical understanding of planetary-scale flow regimes. *J. Atmos. Sci.,* **50,** 1792–1818.

Robinson, W. A., and J. Qin, 1992: Predictability of the zonal index in a global model. *Tellus,* **44A,** 331–338.

Thompson, D. W. J., and J. M. Wallace, 1998: The Arctic Oscillation signature in the wintertime geopotential height and temperature fields. *Geophys. Res. Lett.,* **25,** 1297–1300.

Toth, Z., and E. Kalnay, 1993: Ensemble forecasting at NMC: The generation of perturbations. *Bull. Amer. Meteor. Soc.,* **74,** 2317–2330.

Tung, K. K., and A. J. Rosenthal, 1986: On the extended-range predictability of large-scale quasi-stationary patterns in the atmosphere. *Tellus,* **38A,** 333–365.

Wallace, J. M., and D. S. Gutzler, 1981: Teleconnections in the geopotential height field during the Northern Hemisphere winter. *Mon. Wea. Rev.,* **109,** 784–812.

Zwiers, F., 1987: A potential predictability study conducted with an atmospheric general circulation model. *Mon. Wea. Rev.,* **115,** 2957–2974.